A hybrid full MAS and Combined MAS/TSA Algorithm for Electromagnetic Induction Sensing

F. Shubitidze [1], K. O'Neill [1,2], K. Sun [1], I. Shamatava [1], and K. D. Paulsen [1]
[1] Thayer School of Engineering, Dartmouth College,
Cummings Hall, HB 8000, Hanover NH, 03755, USA

[2] USA ERDC Cold Regions Research and Engineering Laboratory,
72, Lyme Road, Hanover NH, 03755, USA

Abstract –Electromagnetic induction (EMI) sensing, in both frequency and time domains, is emerging as one of the most promising remote sensing technologies for detection and discrimination of buried metallic objects, particularly unexploded ordinance (UXO). UXO sites are highly contaminated with metallic clutter so that the major problem is discrimination not detection. This requires high fidelity forward modeling for successful inversion and classification. Recently, the method of auxiliary sources (MAS) has been applied for solving a large range of ultra-wideband (1 Hz- 300 kHz) electromagnetic induction problems [1] - [6]. For a highly conducting and permeable metallic object, when the skin depth becomes small (at high frequency, i.e. induction number >100) the efficiency of the MAS is reduced significantly [6]. Other methods are stressed in this region as well. At the same time the Thin Skin Approximation (TSA) [7] - [9], which is based on the divergence free Maxwell's equation in a thin layer, infinitely close to the boundary interior, has shown very accurate results at high frequency/induction number. In this paper a hybrid algorithm, with standard MAS and also the MAS with TSA, is introduced and applied for solving the electromagnetic induction forward problem. Once the broadband frequency domain (FD) electromagnetic response is found it is translated into time domain (TD) using an inverse Fourier transform specialized for the characteristic TD input form. Numerical experiments are performed for highly conducting and permeable canonical objects, illuminated by a magnetic dipole or a loop antenna. These tests indicate that an algorithm using either the full MAS or MAS-TSA formulation, where appropriate, should provide a simulator that is applicable and efficient enough for fast 3-D solutions on a PC, under all conditions across the EMI band in both frequency and time domains.

Keywords: Hybrid, method of auxiliary sources, electromagnetic induction, skin-depth, time domain, frequency domain.

I. Introduction

Efficient and accurate numerical modeling of electromagnetic induction (EMI) responses by metallic objects finds application in many fields and has been a subject of research for some time [10 and references therein]. Recently, interest has been driven in part by the necessity for cleaning up buried unexploded ordnance (UXO). This is a potential problem in perhaps 10,000,000 to 15,000,000 acres within the United States, and is an even more severe problem in other parts of the world where military conflicts have taken place. Even rather distant history, e.g. World War I, has left a large legacy of dangerous and possibly polluting UXO in populated areas [11]. Use of remote sensing for UXO clearance is greatly limited by the fact that it is not possible to detect remotely the explosive contained within a more or less intact metal casing. Therefore, we are left having to interpret signals produced by the metal body itself. These bodies can be quite complex in both geometry and composition. Furthermore, widespread metallic clutter at UXO sites and possibly multiple UXO near one another enormously complicate signal interpretation. For effective target inversion or classification algorithms, one requires very high fidelity, efficient forward models to apply in data processing schemes.

Ultra-wideband (~ 20 Hz to 100's of kHz) electromagnetic induction (EMI) sensors are among the most promising tools for the detection and discrimination of buried UXO [1] - [9], [11] - [30]. Most metallic objects produce broadband responses; different metals also produce different responses in the EMI band; and clutter is prominent. Therefore, one must resort to processing broadband data from many different looks at an unseen object, to achieve sufficient information diversity to classify targets successfully. This places a great burden on processing and the associated modeling, which has driven the development of new analyses and analytical tools for studying EMI scattering problems. The only well established analytical solutions to date for broadband EMI scattering are for the case of the sphere in both frequency and time domain [31], [32] and cylinder of infinite length oriented transverse to the primary field [33]. Recently progress has been reported for analytical solution of EMI scattering from spheroids [34], [35], including specialization to treat high frequency conditions, when penetration of the object is slight [35] using the small penetration approximation (SPA). Remaining evaluation problems for the spheroidal shapes in the mid-induction number region of the EMI band have recently been solved using asymptotic methods [36], so that a relatively complete analytical solutions for spheroids are now available. Particularly for arbitrary 3-D geometries, one must usually resort to numerical models to obtain results most relevant to the variety of target types that must be considered. Targets of arbitrary shape have been attacked using the Method of Moments (MoM) with an impedance boundary condition (IBC) [19]. More recently, bodies of revolution (BOR) have been modeled using the MoM with full, rigorous boundary conditions, requiring substantial computation times [14]. Hybrid finite element method (FEM) –boundary element method (BEM approaches not reliant on the IBC have also been developed [23] – [24]. In the FD, a compact numerical formulation has been produced for arbitrary shapes using the Thin Skin Approximation (TSA) [7] - [9], which only applies the divergence equation for magnetic field inside the target.

This performs very well for the difficult realm of high frequency conditions, and for high permeability cases has remarkably broadband applicability. The decision whether to apply a full numerical treatment of the problem or one of the small penetration formulations (TSA, SPA) is most easily made in FD approaches, where skin depth is fixed for a given material and frequency. However a parallel system has also succeeded in direct TD formulations [37]. In what follows, we will pursue only the FD-TSA, converting to TD by inverse Fourier transform (FT).

Most recently, the authors have developed the Method of Auxiliary Sources (MAS [1] - [6]) for numerical solution of the full EMI problem for penetrable, highly conducting and permeable metallic targets. The MAS was originally designed for solving various electromagnetic radiations and scattering problems [38 and references therein]. Later, it was successfully combined with the SPA [6] and TSA [39] for analysis of EMI scattering phenomena. In the standard MAS for EMI [1], boundary value problems are solved numerically by representing the electromagnetic fields in each domain of the structure under investigation by a finite linear combination of analytical solutions of the relevant field equations, corresponding to sources situated at some distance away from the boundaries of each domain. The "auxiliary sources" producing these analytical solutions are chosen to be elementary currents/charges located on fictitious auxiliary surface(s), usually conforming to the actual surface(s) of the structure. In practice, at least as the method is realized here, we only require points on the auxiliary and actual surfaces, without resorting to the detailed mesh structures as required by other methods (FEM, BEM, etc).

EMI scattering responses are often expressed relative to the induction number $\chi \equiv \sqrt{\sigma\omega\mu}\, a$, where a (m) is a characteristic dimension of the object (usually the smallest one), ν = frequency (Hz), $\mu = \mu_o\mu_r$ is magnetic permeability [H/m] and σ (S/m) is the scatterer's electrical conductivity. (The time dependence expression $e^{j\omega t}$ is assumed and its expression suppressed in all FD equations that follow, where j is the square root of minus one, t is time (s), and ω is 2π times frequency in Hz). The quantity χ is proportional to a/δ, where δ is the skin depth, and serves as a dimensionless, scaled frequency.

While we have shown various advantages of the MAS for the EMI scattering problem, its main limitation is reduced accuracy and efficiency at the high frequency end of the EMI band [9]. This is because the influence of source entities sought in the solution decays over a distance of a few δ, which becomes very small at high frequencies (induction numbers). That distance becomes much smaller than the mesh spacing, when the numerical resolution is only fine enough to represent the object shape accurately. This means that without intolerably fine meshing the source quantities sought cannot interact; many matrix elements become almost zero (within the accuracy of the computer); the matrix becomes ill-conditioned and the solution unstable. The same problem arises whether one places the unknown sources

mathematically on auxiliary surfaces, or on the physical surfaces, as in popular integral equation techniques.

To avoid this kind of difficulty, several types of approximations were developed recently, including the TSA and SPA, which are related to impedance boundary conditions. The accuracy and validity of the TSA in conjunction with the BEM have been studied previously [9], in application to highly conducting and permeable (e.g. steel) metallic objects with regular geometries, such as the sphere, ellipsoid, prolate, and oblate spheroid, subject to a uniform primary magnetic field. Under these constraints it has been shown that, for a wide class of EMI scattering problems, the TSA is very accurate and efficient over the entire broadband EMI frequency range [9]. It is easy to implement for an arbitrary geometry. At the same time, the BEM-TSA cannot treat low induction number cases reliably, particularly for non-permeable materials. Recently, a hybrid MAS-SPA algorithm was developed in [6]. It has been shown that MAS-SPA is very efficient for analyzing EMI responses at high induction numbers for spheroidal objects. The algorithm employs a factor f (see eq. 56 in [35]) that can readily be obtained for spheroidal shapes. However, it is very difficult to extend this algorithm for arbitrary geometries. Later the combined MAS/TSA algorithm was introduced and tested for highly permeable and conducting regular shapes under highly variable primary (transmitted) fields as well non-regular geometries [39]. Here we introduce a hybrid MAS – MAS/TSA system, in which the algorithm switches between the full MAS and the MAS/TSA as needed.

Many EMI sensors operate in the time domain (TD), with transmitted signals that are approximately step functions. They are designed to record only during the time immediately after the steady transmitted field has been shut off (the "turn off" case). Here an inverse Fourier transform is used to obtain transient TD response from the FD MAS – MAS/TSA solution for a highly conducting and permeable metallic object, for both turn-on and turn-off cases. A fast and reliable algorithm for the inverse transform has been developed, specialized for the step function input. It treats a singularity in the integrand effectively, even for relatively sparse data points. Because the MAS – MAS/TSA algorithm can operate stably, accurately, and efficiently from the lowest (~static) to the highest (~PEC) EMI frequencies, sufficient bandwidth is achieved in the numerical solutions so that FD results can be inverted into TD without perturbations, even in the most extreme time ranges.

The full MAS formulation applied at low frequencies only requires modest numerical resolution, on the order of that to define the geometry. In the combined MAS/TSA algorithm applied at higher frequencies, only about the same order of resolution is required, while the number of unknowns is reduced by a factor of 3 in 3-D problems. Single frequency computations are approximately four times faster. For multi-frequency cases, the matrices expressing magnetic fields produced by auxiliary magnetic charges do not depend on frequency and can be stored for use, without recalculation, over an extended band. Most important, the thorough investigation of numerical experiments clearly shows superior stability, computational speed, and robustness of the hybrid

MAS – MAS/TSA algorithm relative to the standard MAS method at high induction number.

II. Governing equations

2.1 The magneto-quasistatic assumption

All solutions in this study are based in part on two reasonable assumptions. The first is that, throughout the entire UWB EMI frequency band, electromagnetic phenomena are magneto-quasistatic. While this may be taken as something of a foregone conclusion in low frequency EMI, we examine the assumption explicitly here because recent developments have raised the upper frequency limits for EMI practice to about 300 kHz. This makes the magneto-quasistatic assumption more suspects. The second assumption, also examined here, is that electrical currents induced in surrounding soil have a negligible effect compared to those in the (substantial) metal target.

Consider a highly conducting and permeable metallic scattering object, with permeability $\mu = \mu_r \mu_0$ and conductivity σ [S/m] embedded in a uniform background. The time dependence expression of $e^{j\omega t}$ is suppressed subsequently. The governing equations that form the basis for any pertinent analysis of EMI scattering physics are Maxwell's equations. In both static and transient fields, Maxwell's magnetic field divergence equation must be satisfied

$$\nabla \cdot \mathbf{H} = 0. \tag{1}$$

This form of the equation assumes spatially uniform μ. In practice here we will assume that μ may vary between different portions of an object of interest, but that it is constant within any given section or sub-region. Thus (1) applies within every (sub)region, except on boundaries, where we apply a boundary condition instead.

The particular equations in Maxwell's complete set that pertain most directly to induction are Faraday's and Ampere's Laws,

$$\nabla \times \mathbf{E} = -j\mu\omega\mathbf{H}, \tag{2}$$

$$\nabla \times \mathbf{H} = \sigma\mathbf{E} + j\varepsilon\omega\mathbf{E}. \tag{3}$$

Here $\mathbf{E}$ is the electric field (V/m) and $\mathbf{H}$ is magnetic field (A/m). The quantity $j\omega\varepsilon\mathbf{E}$ is called the displacement current, where ε is the permittivity of the medium (farad/m). Note that, even in the frequency domain, ε as used here does *not* include any portion resulting from the electrical conductivity of the medium, σ, the effects of which will always be expressed separately. The term $\sigma\mathbf{E}$ represents conduction electric currents in the medium. We wish to examine the magnitudes of these terms, relative to each other and also relative to the various derivatives on the left side of the equation. We will do this by tracing the influence of each of the terms on the right hand side within an equation entirely in $\mathbf{H}$, obtained by

combining (3) with other of Maxwell's equations. Taking the curl of (3) and performing manipulations yields

$$\nabla^2 \mathbf{H} = j\omega\sigma\mu\mathbf{H} - \omega^2\varepsilon\mu\mathbf{H}. \tag{4}$$

The first and second terms on the right in (4) descend from the first and second terms on the right in (3), respectively. Specifically, the relative magnitude of the first (second) term on the right hand side of (3) corresponds to the relative magnitude of the first (second) term on the right hand side of, (4) and we will analyze them latter. The three parameter regions where this equation will be examined are those for air (free space), the soil, and the metallic scatterers.

The situation is different in each of the three parameter regions. In the air we assume that σ is approximately zero, so that the second term in (4) drops out. This leaves a classical wave equation with wavenumber k defined as

$$k = \frac{2\pi}{\lambda} = \omega\sqrt{\varepsilon\mu} \tag{5}$$

where λ is the wavelength.

At the top of the MF-EMI band (300 kHz), this expression indicates that the electromagnetic wavelength is one kilometer. Typical distances over which we are concerned about electromagnetic interactions are on the order of 1 m. Thus there is negligible phase difference between different points within the domain of consideration in the air. Fields change essentially in unison throughout, with the structure of static fields, gaining time dependence only through the action of sources and boundary conditions. This results in the uniform time factor $e^{j\omega t}$, and a quasi-static phenomenology. The ultimate significance of this in connection with the equations above is that *both* terms on the right hand side of (4) are negligible, as both are FD expressions for time derivatives. Thus the corresponding terms in (3) are also negligible, and the H field is irrotational ($\nabla \times \mathbf{H} = 0$). An irrotational field may be represented as the gradient of a scalar potential, ψ (A)

$$\mathbf{H} = -\nabla\psi. \tag{6}$$

Substituting (6) in (1) produces the governing equation for the air region

$$\nabla^2\psi = 0. \tag{7}$$

Within the soil, σ is nonzero and the ratio of the magnitude of the third to the second term in (4) is $\omega\varepsilon/\sigma$. As a "worst" case, i.e. the one that most threatens the MQS assumption, we assume $\omega \sim 10^6$ rad/s, $\sigma \sim 10^{-2}$ S/m, and $\varepsilon \sim 10^{-10}$ F/m. This combination of parameters means that we would be operating at the extreme upper limit of the MF-EMI band and presupposes a particularly unlucky set of soil properties, with low conductivity but rather high dielectric constant. Even this combination of parameters implies that the third (displacement

current) term is not larger than the second (electric current) term. To estimate the significance of the electric currents in the soil, compare their magnitude to those induced in the metallic target. By general continuity conditions, the electric field **E** will be on the same order in the soil immediately surrounding the target and in the parts of the metal where the most significant currents are flowing. As the currents are equal to σE, the ratio of currents in metal and soil will be approximately equal to the ratio of their conductivities. A reasonable upper bound on soil conductivity is $\sigma \sim 10^{-2}$ S/m. A typical metal of interest has $\sigma \sim 10^{7}$ S/m. Thus the currents in the metal are about nine orders of magnitude stronger than those in the soil. Unless the metal scatterer is extremely small and simultaneously the sensor samples an enormously larger volume of soil (not the case here), the fields in the soil will be dominated by those produced by currents in the metal. That is, the electric currents in the soil will not be a significant factor in determining the fields in the soil. Thus we conclude that the term containing the soil currents may be dropped (first term on the right in (4). We have already concluded that the second term is not more significant than the first; therefore the entire right hand side of (4) is again negligible. Thus, in the soil as in the air, we conclude that the magnetic fields are irrotational and can be represented using a scalar potential, i.e with the governing equation (7). Representing of the magnetic field by the scalar potential ψ, instead of a vector potential, has two main advantages: first the calculation of Greens function related to the Laplace equation (7) is very simple and fast, and second the scattered magnetic field can be represented as summation of the fields produced by a set of magnetic charges. This reduces number of unknowns at least a factor of 2 relative to the vector potential representation.

Within the metal, we again examine the quantity $\omega\varepsilon/\sigma$. Using the typical values cited above we immediately conclude that the displacement current term is negligible compared to the electric current term. However, the electric currents within the metal are by no means negligible; rather, they are a fundamental source of the scattered signals. Thus two terms remain in (4), which may be constructed as a Helmholtz equation

$$\nabla^2 \mathbf{H} + k^2 \mathbf{H} = 0, \quad k = \sqrt{-j\omega\sigma\mu}. \qquad (8)$$

Here k is sometimes referred to as a wavenumber, by analogy with higher frequency solutions to the equation. However, note that (8) is *not* a wave equation, as the second term $-j\omega\sigma\mu\mathbf{H}$ is the frequency domain equivalent of $\sigma\mu$ times the *first* derivative of **H** with respect to time, not the second derivative. We can generate traveling undulations within the metal by imposing sinusoidal behavior on its surface. However these are not true waves, e.g. they do not reflect. As in the wave case, fundamental solutions of (8) can be expressed as

$$\mathbf{H} \sim \frac{e^{jkR}}{\mu_r R}, k = \gamma + i\gamma \,, \ \gamma = \frac{\sqrt{\omega\sigma\mu}}{\sqrt{2}}, \ \mathbf{R} = \mathbf{r} - \mathbf{r}'. \quad (9)$$

Because the real and imaginary parts of k are equal, the spatially oscillating factor e^{jkR} decays by $1/e$ in less than one sixth of its spatial period.

2.2 The method of auxiliary sources

In the EMI frequency regime the EM fields penetrate the scatterer, at least to some degree. Internal and external fields at the surface of the object must satisfy the continuity of tangential components of **H** and normal component of **B**

$$\hat{\mathbf{n}} \times (\mathbf{H}_1^{sc} + \mathbf{H}^{pr}) = \hat{\mathbf{n}} \times \mathbf{H}_2, \qquad (10)$$

$$\hat{\mathbf{n}} \cdot (\mathbf{H}_1^{sc} + \mathbf{H}^{pr}) = \hat{\mathbf{n}} \cdot \mu_r \mathbf{H}_2. \qquad (11)$$

Here $\hat{\mathbf{n}}$ is a unit normal vector on the real surface, $\mathbf{H}^{pr}$ is the primary (transmitted) magnetic field, $\mathbf{H}_1^{sc}$ is the scattered magnetic field which we consider to be radiated by the auxiliary magnetic charges, which are distributed over the inner auxiliary surface [1]; $\mathbf{H}_2$ is the total magnetic field inside the object, produced mathematically by the auxiliary magnetic sources placed on the outer auxiliary surface. Using conventional MAS [1] the boundary conditions (10) and (11) can be written in the following compact matrix form:

$$\begin{bmatrix} G_n^Q & \mu_r G_n^{P_u} & \mu_r G_n^{P_v} \\ G_u^Q & G_u^{P_u} & G_u^{P_v} \\ G_v^Q & G_v^{P_u} & G_v^{P_v} \end{bmatrix} \begin{bmatrix} Q \\ P_u \\ P_v \end{bmatrix} = - \begin{bmatrix} H_n^{pr} \\ H_u^{pr} \\ H_v^{pr} \end{bmatrix}. \qquad (12)$$

Here Q is a vector containing the amplitude of auxiliary magnetic charges, P_k, k=u,v is a vector containing the amplitudes of auxiliary magnetic dipoles oriented along u and v, which are orthogonal directions on an auxiliary surface, G_ξ^Q is exterior field expressed with Green's function $1/(4\pi R)$ where $R=|\mathbf{r}\text{-}\mathbf{r}'|$ and $G_\xi^{P\gamma}$ is the interior solution expressed ultimately in terms of dipole sources distributed over an exterior auxiliary surface, together with a Green function of the form $e^{jkR}/4\pi R$. More explicit forms of the G_ξ^Q, and $G_\xi^{P\gamma}$ matrices, where $\hat{\xi} = \hat{\mathbf{n}}, \hat{\mathbf{u}}, \hat{\mathbf{v}}; \gamma = u, v$, are presented in [1]. When the skin depth becomes small so that both real and imaginary parts of k become high, the $G_\xi^{P_k}$ matrix's elements become very small compared to G_ξ^Q matrix elements. At relatively high frequency (more that 10 kHz for common steel, copper, aluminum, brass etc), the $G_\xi^{P_k}$ matrix elements decay very rapidly in space and the system (12) becomes unstable.

2.3 Combination of MAS with TSA

To avoid this problem it is desirable to establish an alternative formulation that would be applicable for high frequencies. It is well known that at high induction numbers the fields in the interior of the scatterer are non-zero only in a thin layer close the surface (Fig. 1). Under this condition, we exploit the divergence free Maxwell's equation applied in that near surface region. That equation and the thinness of the surface layer provide a boundary condition on the external field, obviating the necessity for complete solution of the internal field. We will proceed in a manner analogous to that in [8], [9]. In those references linear interpolation of unknowns is used over piecewise flat surface elements, in a Galerkin integral treatment of the governing relation. Here consider a general curvilinear surface, with completely continuous tangents and normals, and a subdomain integration of the governing equation. Gauss's Law (the magnetic field divergence equation) is integrated over a thin finite volume just below the object's surface, to produce the relation

$$\nabla \cdot \mathbf{H}_2 = 0 \quad \Rightarrow \quad \oint_A \mathbf{H}_2 \cdot d\mathbf{A} = 0, \tag{13}$$

or

$$H_{2,n_2} A_{n_2} - H_{2,n_1} A_{n_1} + H_{2,u_2} A_{u_2} - H_{2,u_1} A_{u_1}$$
$$+ H_{2,v_2} A_{v_2} - H_{2,v_1} A_{v_1} = 0 \tag{14}$$

where $A = A_{n_2} + A_{n_1} + A_{u_2} + A_{u_1} + A_{v_2} + A_{v_1}$ is a total area of the thin volume. Dividing (14) equation by the layer thickness d and take limit as $d \rightarrow 0$ yields

$$A_n \frac{\partial H_{2,n}}{\partial n} + H_{2,n} \frac{\partial A_n}{\partial n} + H_{2,u_2} L_{u_2} - H_{2,u_1} L_{u_1}$$
$$+ H_{2,v_2} L_{v_2} - H_{2,v_1} L_{v_1} = 0. \tag{15}$$

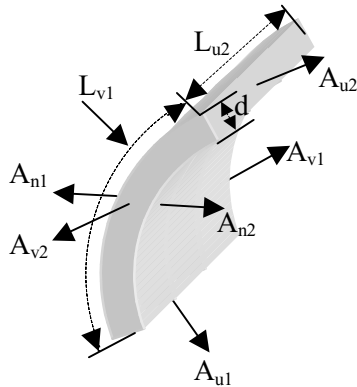Here $\partial n = \partial d$. The basic tenet of the TSA is that fields just

Fig. 1.   Geometry of volume just below the real surface A.

below the surface within the thin layer vary approximately one-dimensionally, normal to the surface. Thus, as d -> 0 the normal component of the magnetic field $H_{2,n}$ and it's derivative $\frac{\partial H_{2,n}}{\partial n}$ along normal $\hat{\mathbf{n}}$ are related to each other through [9]:

$$\frac{\partial H_{2,n}}{\partial n} = jk H_{2,n}(0, u, v) \tag{16}$$

where $H_{2,n}(0, u, v)$ is the value as n->0 on the interior of the surface. Based on the boundary conditions (10) and (11) together with the TSA condition (16), equation (15) can be rewritten for external magnetic field on boundary in a form involving only quantities on the surface:

$$\left[H_{1,n}^{sc} \frac{1}{\mu_r} \left(jk A_n + \frac{\partial A_n}{\partial n} \right) \right] +$$
$$\left[H_{1,u_2}^{sc} L_{u_2} - H_{1,u_1}^{sc} L_{u_1} + H_{1,v_2}^{sc} L_{v_2} - H_{1,v_1}^{sc} L_{v_1} \right] = -[Y], \tag{17}$$

or, in matrix form:

$$[Z][Q] = -[Y]. \tag{18}$$

Here

$$[Z] = \left[G_n^Q \frac{1}{\mu_r} \left(jk A_n + \frac{\partial A_n}{\partial n} \right) + G_{u_2}^Q L_{u_2} - G_{u_1}^Q L_{u_1} \right] +$$
$$\left[G_{v_2}^Q L_{v_2} - G_{v_1}^Q L_{v_1} \right], \tag{19}$$

and

$$[Y] = \left[H_n^{pr} \frac{1}{\mu_r} \left(jk A_n + \frac{\partial A_n}{\partial n} \right) \right] +$$
$$\left[H_{u_2}^{pr} L_{u_2} - H_{u_1}^{pr} L_{u_1} + H_{v_2}^{pr} L_{v_2} - H_{v_1}^{pr} L_{v_1} \right]. \tag{20}$$

When the near-surface layer of electromagnetic activity is sufficiently thin relative to object dimensions (a/δ ~ 0.1 or less), the equations above are completely sufficient to include the interior response of the target and to connect it to the exterior fields. To apply MAS to the exterior region, a set of magnetic charges is placed mathematically inside the physical surface, on the auxiliary surface S_1^{aux} shown in Fig. 2. The secondary magnetic field due to the target is expressed as a superposition of the fields generated from a finite number (N) of point charges, $\{Q_i\}$, $i = 1, 2, 3, ..., N$ placed on the surface S_1^{aux}. The total secondary magnetic field at the position $\vec{r}_n$ due to the auxiliary charges is expressed as Eq.
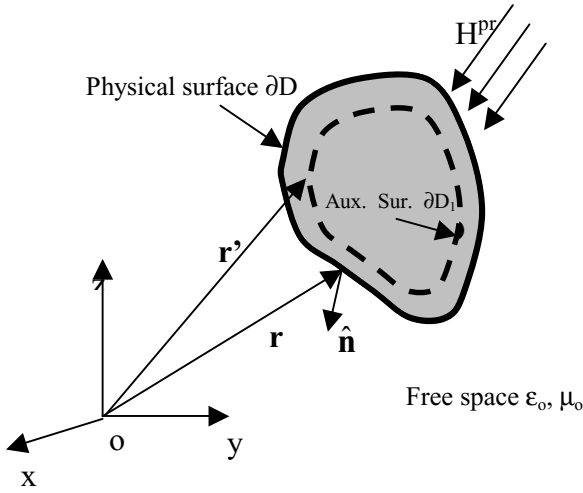
Fig. 2. Combined MAS-TSA.

(21) in [1]. By applying equation (17) at M collocation point on S and expressing $\vec{H}_1^{sc}$ using the $\{Q_i\}$, we cast into an NxM linear system of equations, where normally we set M=N.

The significance of all this is that TSA together with standard boundary conditions across the boundary allows us to write the entire problem strictly in terms of *exterior* field quantities (17). These in turn can be solved for in terms of a simple set of *scalar* auxiliary source strengths, distributed relatively sparsely over an auxiliary surface. We term this formulation the combined MAS-TSA algorithm, because it retains an MAS formulation for the exterior field, but treats the interior field only through the TSA. The "full MAS" designates an MAS formulation applied to both interior and exterior regions. One can also mix MAS and TSA in another sense, namely applying the full MAS under conditions where it is appropriate, and easily switching to the combined MAS/TSA where it is appropriate, e.g. at higher frequencies. This provides a full EMI band simulator, essentially from the magneto-static lower limit to the upper PEC limit at some 100's of kHz.

2.4 Transient response of a highly conducting and permeable object

TD EMI instruments have been very prominent in localized subsurface surveying, particularly for detection and discrimination of UXO [40 and references therein]. The transient response can be obtained from the MAS –MAS/TSA FD solutions by an inverse Fourier transform

$$H(t) \;=\; \frac{1}{2\pi}\int\limits_{-\infty}^{\infty} H(\omega)H^{pr}(\omega)e^{j\omega t}d(\omega). \qquad (21)$$

Here ω is angular frequency and $H(\omega)$ is the FD solution. In measurement practice, the primary magnetic field is typically a downward step function

$$H^{pr}(t) \;=\; H_o^{pr}\,u(t) \qquad (22)$$

where

$$u(t) = \begin{cases} 1,\ t<0 \\ 0,\ t\geq 0 \end{cases}$$

which corresponds to the "turn off" case. In the FD

$$H^{pr}(\omega) = H_o^{pr}\sqrt{\frac{\pi}{2}}\left(\frac{1}{j\pi\omega} + \delta(\omega)\right). \qquad (23)$$

III. Numerical Results

In this section the hybrid standard MAS and combined MAS/TSA method are applied to the analysis of broadband electromagnetic scattering by highly conducting and permeable metallic objects. The validity and sensitivity of TSA in conjunction with the BEM method has been widely tested for canonical geometries under time varying uniform field [9]. While we expect the underlying approximation to produce an accurate system at sufficiently high induction numbers, past BEM/TSA experience suggests that applicability may be wider than that, depending on the scatterer's permeability. Therefore, we will perform numerical tests of the new method across the entire EMI band. The results are compared with a solution obtained by full (conventional) MAS and experimental data obtained using the
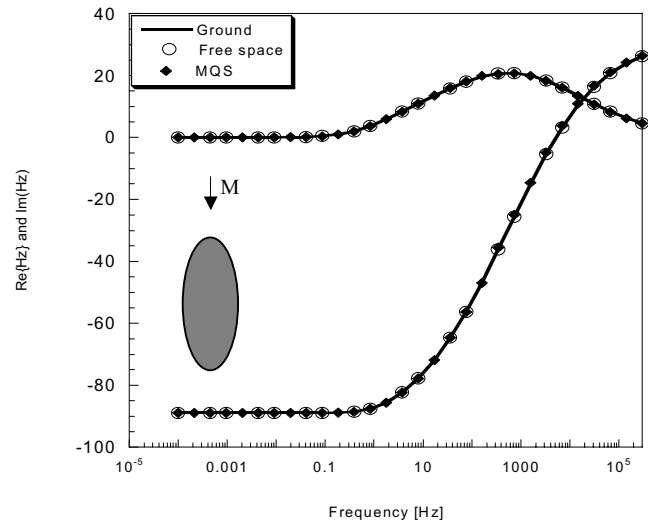

Fig. 3. Scattered magnetic field versus frequency, for a spheroid.

GEM-3 sensor [41]. All MAS calculations described below were done with the simplest point matching, point source code [1]. Finally, transient TD EMI responses are simulated and analyzed for highly conducing, permeable and non-permeable spheroidal objects.

Validity of MQS assumption

First we perform calculations to check the validity of the MQS assumption over the entire EMI band. A prolate spheroid, with minor axis $a=10$ cm, major axis $b=50$cm, and conductivity $\sigma = 10^7$ S/m and relative permeability $\mu_r = 100$, is excited by a magnetic dipole placed above it. The distance between the center of the spheroid and dipole is 60 cm. Fig. 3 shows the scattered magnetic fields versus frequency for three

permeable and non-permeable spheres, illuminated by an oscillating magnetic field from a loop antenna. The radius of the sphere is $a =10$ cm, with electromagnetic parameters $\sigma=4\times10^6$ [S/m] and $\mu_r = 1$ or 150. The field produced by the multi-loop antenna is described in detail elsewhere [41], [5]. The distance between the antenna's center and top part of the sphere is 5cm. The observation point is at the center of the antenna. The co-planar, concentric inner and outer loop radii are 10 cm and 20 cm, respectively. The current amplitudes and

TABLE I: MAS and hybrid MAS-TSA complexity for the generation of the results in Fig.4 Computation was done on Pentium IV, 2 GHz speed.

Induction number range	Standard MAS $\mu_r = 1$		Standard MAS $\mu_r = 150$		Combined MAS-TSA any μ_r	
	Number of unknowns	CPU Time (secs)	Number of unknowns	CPU Time (secs)	Number of unknowns	CPU Time (secs)
0< ka<10	40	0.15	60	0.25	14	0.015
11< ka<100	60	0.25	120	1.12	14	0.015
101< ka<1000	80	0.52	280	5.8	14	0.015

cases. In the first case, the spheroid is placed in a uniform ground with conductivity $\sigma = 10^{-2}$ S/m and simulation is done including a displacement and electric currents, both within the object and outside it (no MQS assumption, solid line in the figure). The second case assumes that the spheroid is placed in free space and again simulation is done without MQS assumption (circles). Finally, a third case employs the MQS assumption throughout (no electric currents in surrounding space, no displacement currents throughout: diamonds). In all

their directions on the loops are chosen in such way that at the centers of the loops the primary field is zero. Fig. 4 shows comparisons of scattered magnetic field calculated by standard MAS [1] with number of sources N and by the combined MAS-TSA [39], both with formulations assuming a body-of-revolution (BOR). The figure shows the "full" range of induction numbers in that the problem ranges from lowest values of interest, in which the primary field penetrates the object completely (~ magnetostatic case), up to asymptotic
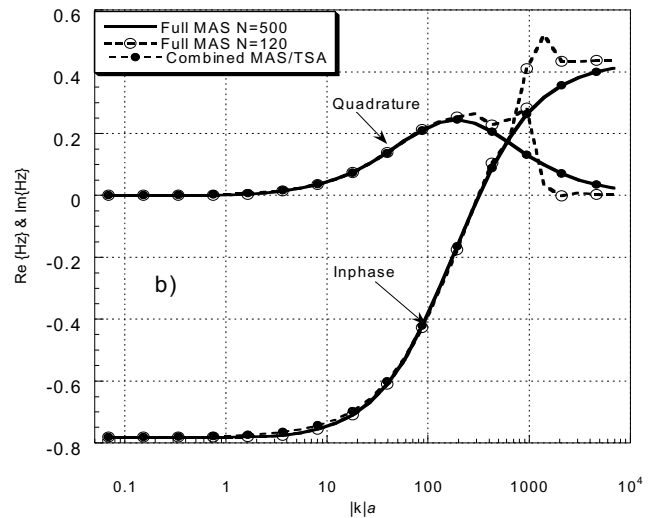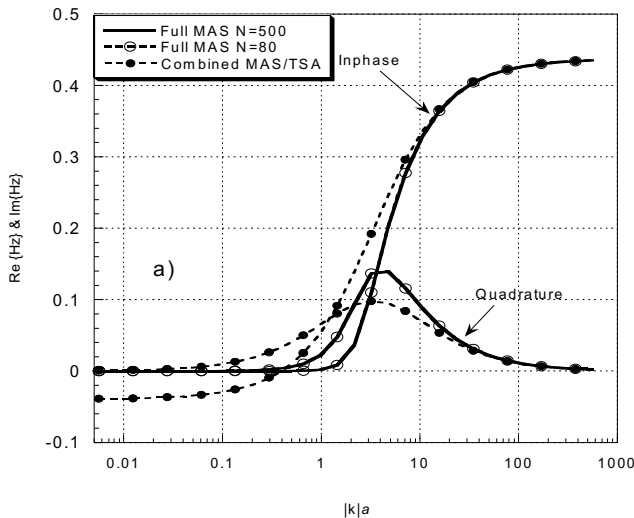

Fig. 4. The scattered magnetic field versus induction number for sphere subject to a realistic sensor: a) non-permeable, b) permeable case.

three cases the scattered magnetic fields for the spheroid are the virtually the same, i.e the MQS assumption is very accurate across the entire EMI frequency range.

1. *Accuracy and Complexity of combined MAS-TSA algorithm for non-uniform excitation*

Next we examine the performance of the two formulations for simulating EMI scattering from highly conducting,

high frequency limits, with arbitrarily small skin depth (~ PEC case). At low induction numbers the full MAS gives high accuracy results compared to the combined MAS/TSA method for the non-permeable sphere. As induction number increases, this difference becomes insignificant (in these cases, as in the BEM-TSA [7] – [9] in cases with uniform fields, when the induction number is more than about 20). For the highly permeable sphere the full MAS with relatively dense distribution of sources and combined MAS/TSA algorithm are

in very good agreement over the entire band. However, the standard MAS with small number of sources becomes unstable (Fig. 4 b) after induction number 100, which is not the case for non-permeable sphere (Fig. 4 a). This means that, at any particular resolution, the stability of the full MAS is determined by two factors: induction number and permeability. Both these parameters affect the matrix elements $G_\xi^{P_k}$ in equation (12) in approximately the same way. Thus,

8000 with no apparent difficulties associated with change in skin depth and associated resolution requirements.

Comparisons between CPU time and source density for two standard MAS and combined MAS/TSA solutions are given in table I. For full MAS solution of the same problem at high induction number (single frequency) approximately from 6 to 12 times more unknowns were required. However, depending on the object geometry, a much higher number of unknowns may be necessary to achieve convergence of the solutions
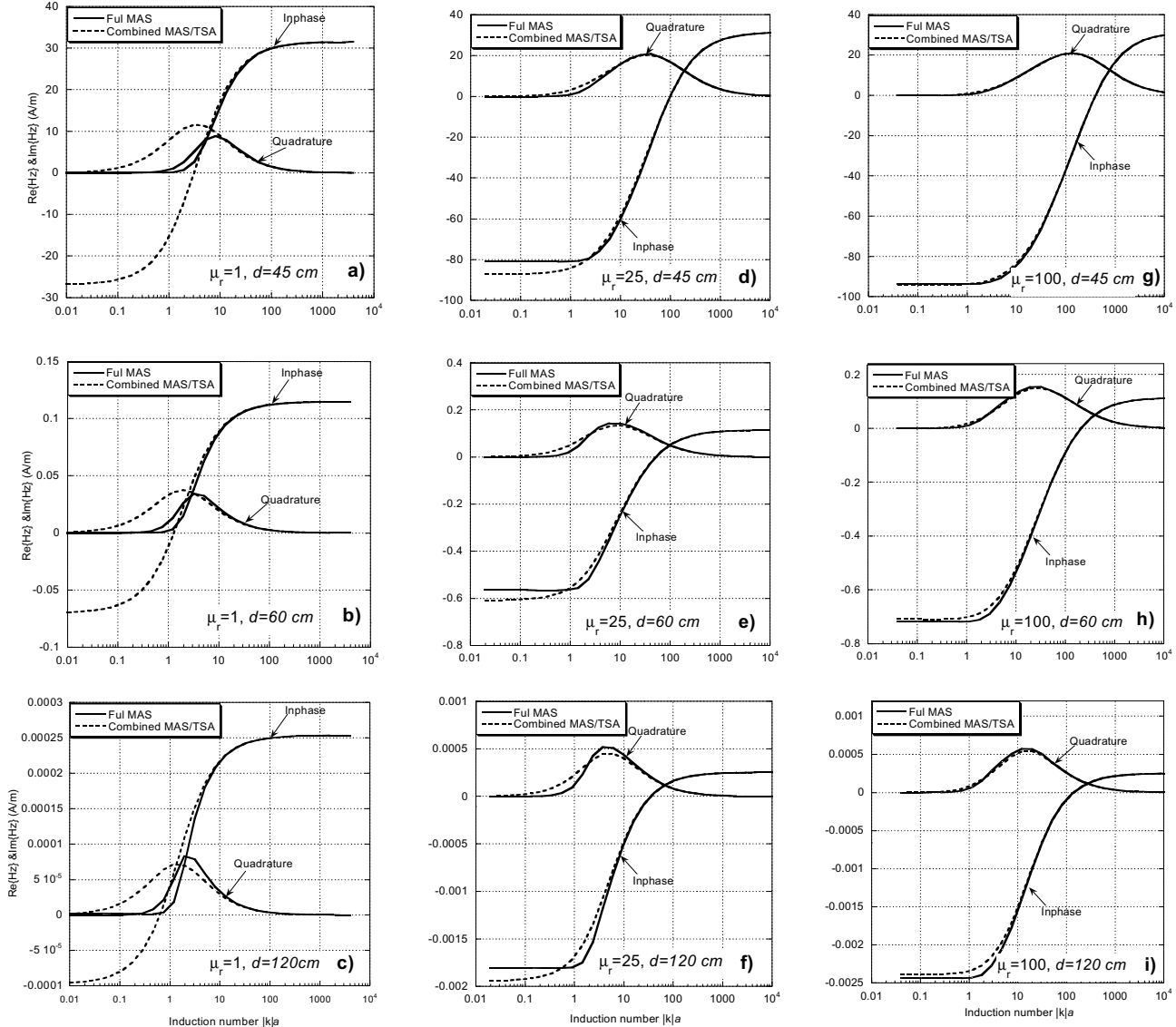

Fig. 5. The scattered magnetic field versus induction number for a prolate spheroid.

when these parameters increase, the total magnetic field $\mathbf{H}_2$ inside the object decays steeply, interaction between the discretized quantities degenerates, and the system (12) becomes unstable. At the same time, the accuracy of combined MAS/TSA algorithm significantly increases at low induction numbers for high permeability (Fig. 4 b), as in the BEM-TSA [7] – [9] in cases with uniform fields. For the highly permeable case, the MAS/TSA covers the whole band from induction number 0.01 up through induction number

from the standard MAS. In the comparisons between CPU time shown, it is obvious that the reduction in complexity resulting from use of MAS/TSA for this problem is dramatic and becomes more significant as: 1) the induction number increases, and 2) the permeability of the object increases. Note here that results in Table I show two very significant facts, applicable at least to spherical scatterers:

1. For the high permeability objects the accuracy of the MAS/TSA method is reasonably good over entire broadband electromagnetic induction range.

2. To obtain highly accurate results for high permeability objects, the full MAS method requires a very dense distribution of unknowns, which dramatically increases computational time and computer resource requirements.

Compared to conventional MAS, the MAS/TSA algorithm has several features that make it attractive to a wide range of EMI problems. The number of unknowns in MAS/TSA is reduced by a factor of 3 in general 3D EMI problems (see equations (12) and (18)). In the MQS regime, the scattered field is very smooth. This allows the MAS/TSA method, with very low computational cost requirement, to get highly accurate results with a point source/point matching technique, with only the mesh density that is required to represent the geometry accurately. The matrix that produces the scattered field associated with magnetic charges in (17) does not depend on the frequency. Within its realm of validity, MAS/TSA should be much more attractive compared to other numerical techniques such as MoM [14] and FEM, e.g. [23], [24]). The greatest advantages of combining the MAS and MAS/TSA is accuracy over all EMI frequencies for all electromagnetic parameters, with quite simple programming, especially relative to sophisticated MoM type techniques such as the Fast

in b), e), h); and 120 cm in c), f), i) The solid line corresponds to full MAS with N=500 number of sources and dashed line to MAS/TSA algorithm. These figures demonstrate in cases that, when the induction number is more than about 20, both techniques produce virtually the same results. However, at low frequency for non-permeable cases, the MAS/TSA algorithm produces significantly different results (Fig. 5 a-c). These errors are reduced as the dipole moves from the object. Again, as permeability increases the differences between standard MAS and MAS/TSA algorithm become insignificant over the entire EMI frequency range, particularly for μ_r=100, e.g. Fig. 5 g. As the dipole moves from the object with permeability 100, the error between MAS and MAS/TSA become slightly worse, but not significantly. These results also show that depending on the distance between the target and sources of excitation the frequency spectrum of the scatterer is different. This contrasts with the observation in [8], where frequency response is independent of observation point, but under a uniform primary field. For example, for the highest permeability spheroid the peak of the quadrature or imaginary part, associated with volume currents, moves from induction number 100 to 10. It is obvious, that when dipole is close to the object it excites strong eddy currents within the closest part, and in turn these currents will dominate the received signal. When the source is close to the end of the spheroid, its response is reminiscent of that from a sphere, both in terms of performance of the MAS/TSA and in
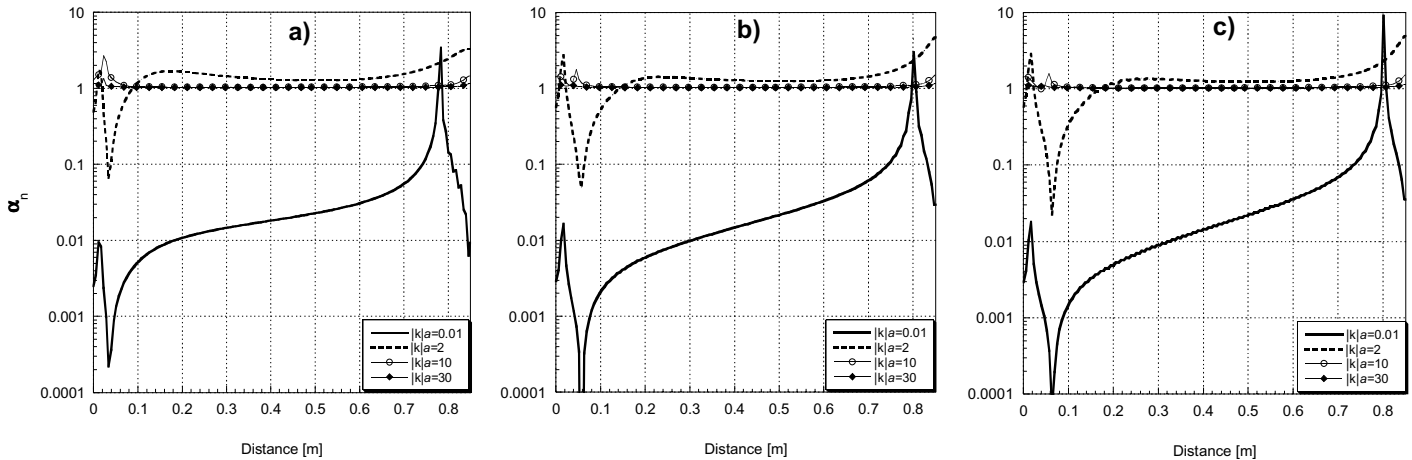

Fig. 6. Error criteria α_n versus distance along surface of the spheroid for permeability a) μ_r=1, b) μ_r=25, and c) μ_r=100.

Multi-pole Method [42].

To check the accuracy of the MAS/TSA algorithm in non-spherical cases, we examine EMI scattering from both non-permeable and permeable prolate spheroids. The spheroid's major to minor axis aspect ratio is four ($b/a = 4$) and minor axis is $a = 10$ cm. It is excited by an axially oriented magnetic dipole placed outside the spheroid on its axis of the symmetry. EM parameters are $\mu_r = 1, 25, 100$. Results are shown relative to induction number $|k|a$, so that $\sigma = 4 \times 10^6$ S/m does not appear explicitly.

Fig. 5 shows results for μ_r=1 (a-c); μ_r=25 (d-f); and μ_r=100 (g-i). The dipole sources are placed at three different distances from the spheroid's center: 45cm in a) d), g); 60 cm

location of peak response. As the source moves away, the geometrical heterogeneity of the object has more effect on the accuracy of the MAS/TSA, and the overall response is more like what we should expect from an elongated magnetic object, axially oriented relative to the primary field [1].

2. Error analysis

To analyze the performance of the MA/TSA code we studied the accuracy of the TS assumption within the object, infinitely close to the surface. In [9], the ratio of TSA approximation to the actual derivative of the normal component of the magnetic field $H_{2,n}$ was denoted

$$\alpha_n = \frac{jkH_{2,n}}{\partial H_{2,n}/\partial n} \qquad (24)$$

and provided an error criterion on the surface of the scatterer. A theoretical analysis showed error patterns in both the basic approximation and, sometimes contrastingly, in the resulting scattered field. Analytical relations produced formulas for both the level of error and the sensitivity of the numerical system to error. The analysis was carried out only for spheres and transverse infinite cylinders, in uniform primary fields, for which the analytical relations could be obtained. Here both $H_{2,n}$ and $\partial H_{2,n}/\partial n$ are obtained along the surface of a spheroidal scatterer, using the conventional MAS code, when the source of the primary field is a magnetic dipole. The source is situated on the rotational axis 45 cm from the center of the spheroid.

Fig. 6 shows the ratio of the TSA values and the numerical derivative values as a function of distance along the (interior) surface. For all three permeabilities, at very low induction numbers ($|k|a = 0.01$ and 2) the difference between $jkH_{2,n}$ and $\partial H_{2,n}/\partial n$ is very significant. They are in fact different orders of magnitude. However the comparisons between scattered fields obtained by combined MAS/TSA and standard MAS show different error patterns, relative to the value of μ_r (Fig. 5). To some extent, one sees the same trends as in [9], despite the difference in object geometry and non-uniformity of excitation: high permeability diminishes the consequences of inaccuracy in the TSA. In order to understand this numerical behavior here, let us examine the expressions in (17). The expression in brackets can be divided into two parts: the first part is associated with the normal component of the magnetic field and with the TSA, while second part is related to the tangential components. Examination of solutions shows that the both normal and tangential components of the scattered magnetic field on the boundary of the scatterer become saturated at very low induction numbers (e.g $|k|a < 0.1$) and at correspondingly low frequencies. That is, however much μ_r is increased, the value of $H_{1,n}^{sc}$ and its magnitude relative to the other components cease to change significantly. This means that, as μ_r increases, the contribution of the first part in brackets to the whole system (18) decreases relative to the contribution from the second part. Thus the quality of our approximation of the normal derivative has reduced effect. For all values of μ_r, the TSA and actual $\partial H_{2,n}/\partial n$ values

Fig. 7. UXO.

almost coincide with each other at induction number $|k|a=10$ and 30. Obviously at these induction numbers the combined MAS/TSA and full MAS agree very well in the far fields of Fig. 5.

The error pattern observed here differs from that in [9] in one important respect, namely here we do not see reduced error at the very lowest induction numbers when there is significant error in the middle range of induction numbers. To understand this, note that at very low induction numbers both $\partial H_{2,n}/\partial n$ and $jkH_{2,n}$ approach zero for the spheroid *uniform* primary field excitation. Therefore, while the ratio of $\partial H_{2,n}/\partial n$ and $jkH_{2,n}$ may not be correct, the latter still approximates the former adequately in that both become negligible. However in the non-uniform primary field considered here, $\partial H_{2,n}/\partial n$ does not approach zero at low induction numbers, even in the static condition. For the non-magnetic case, the internal static fields will show the same complexity of spatial variation as the primary field. The assumption of approximately 1-D gradients below the surface, on which (16) is based, will not hold. Overall, while in certain cases high μ_r values may suppress the effects of errors in the TSA at low induction numbers, in general the TSA is designed for high induction numbers. It does not take into account spatial distribution of the normal component of the magnetic field at low frequencies, and neglects its tangential gradients. See also [39] for additional illustrations of low induction number TSA error, caused by more variable geometry.

The most secure general strategy for obtaining very accurate results over entire broadband EMI frequency range is to use the full MAS and for induction numbers less than about 20 and then switch to the MAS/TSA method for higher induction numbers. Alternatively, we can use the validity of the full MAS solution in the interior to check the accuracy of TSA as we proceed upwards in frequency. When we see that (16) has become valid, we can proceed with the combined MAS/TSA for all higher frequencies.

Having established the accuracy and range of validity of the hybrid full MAS - MAS/TSA, we will use it to investigate EMI response for a real UXO, consisting of two parts: a tail with fins (length 8 cm, diameter 3.15 cm), and main part (largest diameter 8 cm, smallest diameter 3.15 cm). The total length of UXO is 26 cm Fig. 7. The primary magnetic field is generated by a GEM-3 sensor [5,41]. Two excitations were considered: 1) Axial, i.e. when the coil axis of GEM-3 is aligned with the axis of symmetry of the UXO, and 2) transverse, when the GEM-3 axis is orthogonal to its axis. For determination of the EM parameters of each section, the UXO was disassembled. For each part the EMI response was measured separately and a recently developed inverse EMI algorithm [43] was used for inferring their EM parameters. Inverted parameters are: for the main part $\sigma = 1.6 \times 10^6$ S/m, $\mu_r = 85$; for tail $\sigma = 2 \times 10^6$ S/m, $\mu_r = 130$. The numerical solution shown as a solid line in Fig. 4 was obtained by combination of conventional MAS at low induction number $|k|a < 20$, and MAS/TSA for $|k|a > 20$. The comparison between measured and simulated data for the UXO is shown in Fig. 8, with
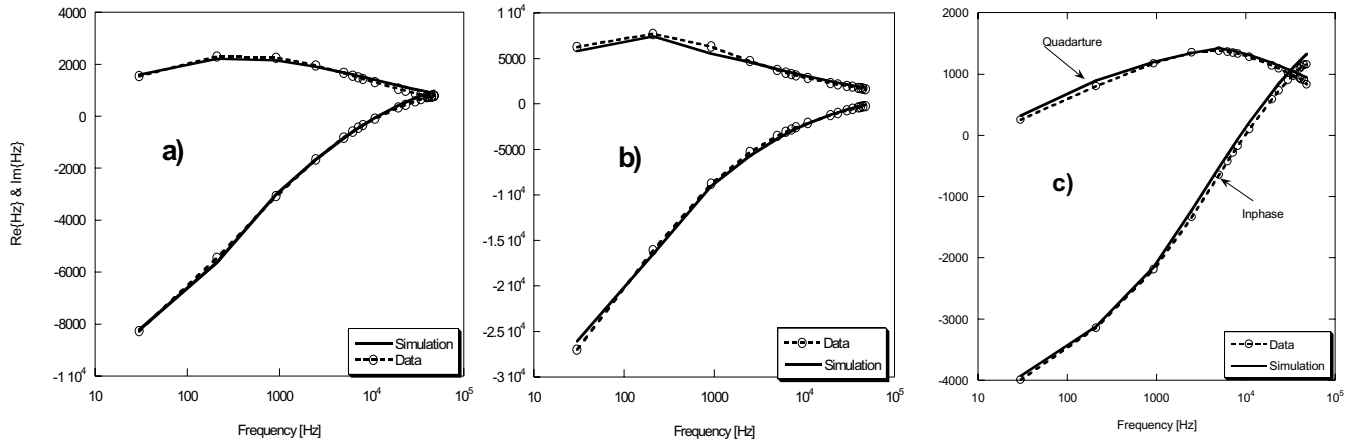
Fig. 8.   Scattered magnetic fields versus frequency for real UXO oriented with (a) the nose up, (b) the tail up, and c) horizontal.

different target orientations. Again agreement is very good. These results clearly show that, depending on the target orientation relative to the sensor's of point of view, the EM responses are quite different. As shown in Fig. 8 a), when the nose is close to the sensor the response behaves like a sphere, whereas when the tail is up Fig. 8 b) the scattered field spectrum suggests the object is elongated (quadrature peak shifted lower, see (5). In the transverse case (Fig. 8 c) the response is more like that of an elongated target in transverse orientation, with quadrature peak at high frequency.

representative of most TD instruments in current use is the "Turn off" case: The initial condition is essentially the steady state solution (unvarying primary field normalized here to unity); at $t = 0^+$ the primary field is shut off and the scattered field is measured. In this case, the calculated response begins at a finite value and decays eventually to zero. For the "turn on" case, the initial condition is zero both inside and outside the object. At $t = 0^+$, the primary field is switched on and the scattered field recorded. A new version of the Geophex GEM-3 sensor will record this case as well as the "turn off." The former may be more revealing than the turn-off case,
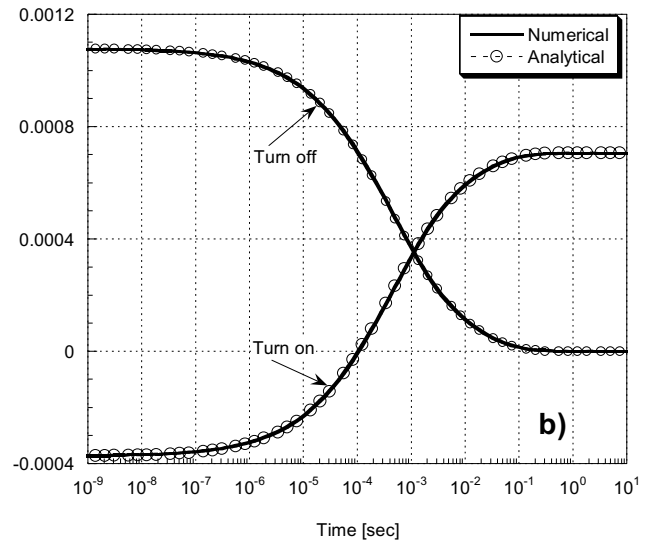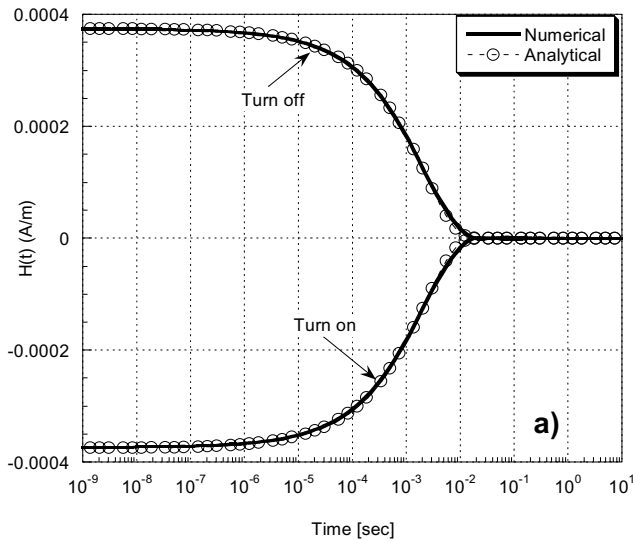

Fig. 9. Transient response for $\mu_r=1$ non-permeable a) and permeable b) $\mu_r=50$ spheres.

3.   Transient response for spheroids

In this section a transient TD EMI response is analyzed for highly conducting and permeable metallic objects, beginning with spheres in both the "Turn on" and "Turn off" TD cases. For checking the accuracy of the numerical method, data are compared against available analytical results. The case

converging in late time to a steady-state value that depends on the object's permeability. The following figure shows example turn-on and turn-off results for a sphere, 5 cm in radius, with electrical conductivity $\sigma = 10^7$ S/m and relative permeabilities 1 and 50, and observation point 1 m distant. Numerical results are compared to analytical values obtained from analytical solutions by James Wait [32].

Note that the beginning value of the turn-off case and the ending value in the turn-on case are not the same. This is because the first response of the object to an imposed change in the surrounding (primary) field is to generate surface currents that oppose the change (Lentz' Law). Thus, in the turn-on case, in which a *positive* primary field value is suddenly imposed, the initial response is *negative*. (See early

b/a=0.25). Fig. 10 shows the scattered magnetic field versus time for turn on and turn off cases, for different permeabilities. Figs. 10a and 10b are for the prolate spheroid illuminated by axial and transverse oriented primary magnetic field, respectively. Depending on the primary magnetic field orientation and spheroid's EM parameters, the decay characteristics are different. The results show that, as
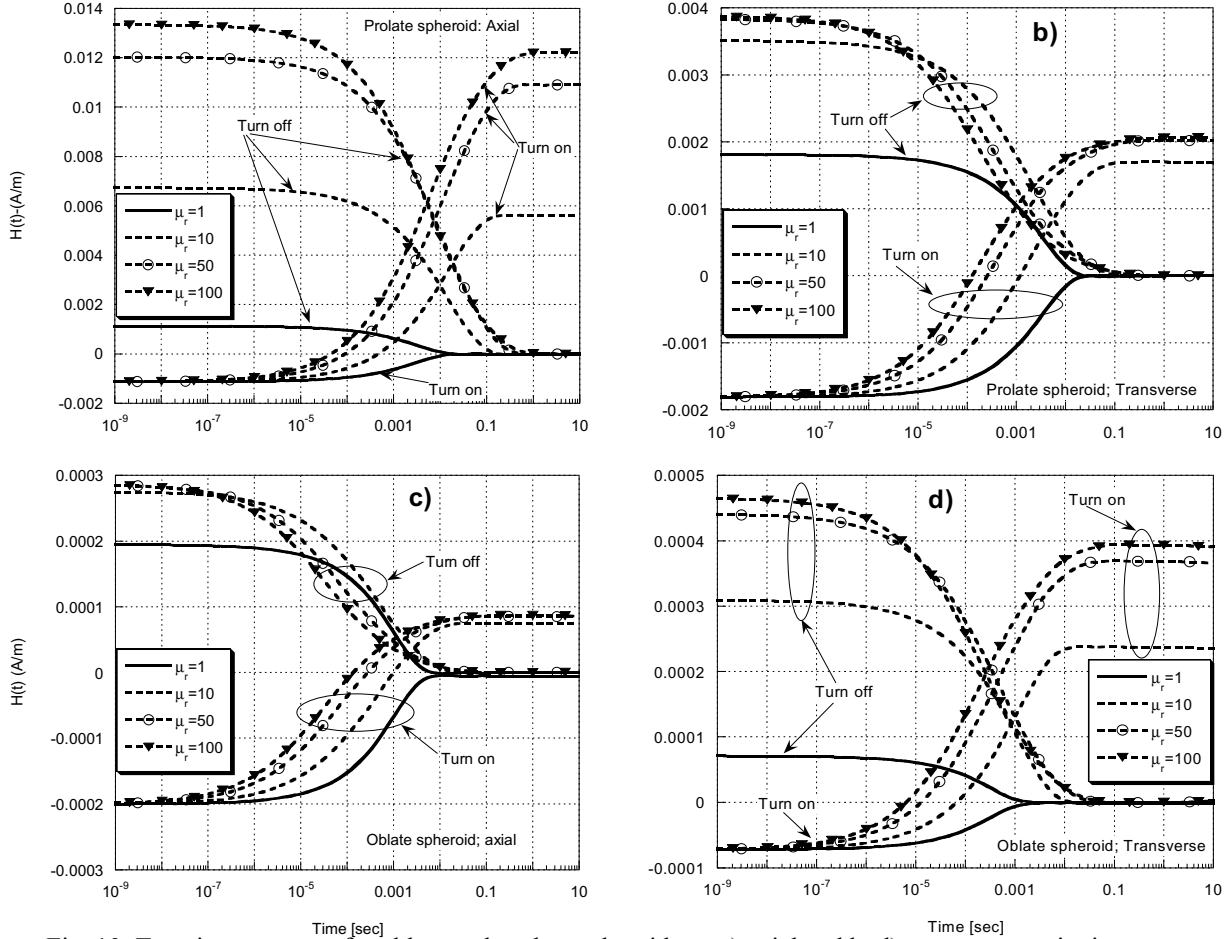

Fig. 10. Transient response for oblate and prolate spheroids, a, c) axial and b, d) transverse excitations.

time in turn-on curve in the Fig. 9). Conversely, in the turn-off case, a *negative* change in the surrounding field is imposed, so the first response of the object is *positive*. In other words, the very early time values seen at the beginning of the turn-off curve (figure above) are not the true steady state response, but are rather steady state augmented by an initial positive response. For the non-magnetic object ($\mu_r = 1$, Fig. 9 a) there is no (non-zero) static response, so the *only* early time response is the initial jump in response to the imposed field. Note that, reassuringly, the change in magnitude of the response from very early to very late time is the same in both turn-on and turn-off cases, for both magnetic (Fig. 9 b) and non-magnetic materials (Fig. 9 a).

Next the transient responses are investigated for highly conducting, permeable and non-permeable prolate (Fig. 10 a,b) and oblate spheroids (Fig. 10. c,d), illuminated by an axial and transverse primary magnetic field. Axis aspect ratios are 4 for both spheroids (prolate b/a=4, a=5cm, oblate

permeability increases, the principal transient response activity (decay curve) shifts earlier in time in both the turn on and turn off cases. Similar behavior of the transient field is observed for the oblate spheroid.

IV. Conclusion

In the paper, an innovative hybrid standard MAS and combined MAS/TSA algorithm is presented for efficiently and accurately analyzing EMI responses by highly conducting and permeable metallic targets. It has been shown that combined MAS/TSA algorithm works most reliably at high induction numbers, where skin depths are very small and more general methods are most stressed. Numerical experiments for a prolate spheroid under highly non-uniform, time varying primary magnetic field have shown that the combined MAS/TSA algorithm is inaccurate at low induction numbers for a non-permeable object. For a highly permeable object, the

MAS/TSA accuracy depends on the primary field, but only slightly, with relatively small errors in the scattered field over the entire band.

These studies suggest that for high accuracy broadband EMI simulation requiring low CPU resources it is necessary to use the standard MAS in low frequencies (induction number less than about 20), and the combined MAS/TSA algorithm at high frequencies (induction number greater than about 20). Accounting for non-uniformity effects at low frequency is particularly important for analyzing near field EMI responses for targets under highly non-uniform primary fields or for multiple, interacting objects, or for objects with very non-uniform geometries. Such cases occur frequently in subsurface unexploded ordinances discrimination problems.

To speed up calculation time it is possible to estimate the accuracy of the TSA via standard MAS, as one proceeds up through the lower frequencies. Then, when it has become valid, we can proceed with the MAS/TSA for all higher frequencies beyond the near static region.

Ultra wideband EMI frequency domain (FD) responses, obtained by the proposed hybrid MAS - MAS/TSA algorithm, are translated in time domain (TD) using a specialized inverse Fourier transform. To validate the FD to TD algorithm, the transient responses for permeable and non-permeable spheres are compared against analytical solutions for both turn on and turn off cases. Numerical TD experiments show that decay characteristics in the transient responses depend of the object geometry, primary field orientation, and EM parameters. For both flattened and elongated shapes, in both axial and transverse excitation, increasing permeability appears to shift the onset of signal decay earlier. From the point of view of discrimination, the turn-on case has the advantage that it may arrive at a non-zero steady state depending on permeability. This may be a more accessible indicator of permeability than signal characteristics near the onset of decay.

V. Acknowledgment

References:

1. F. Shubitidze, K. O'Neill, S. A. Haider, K. Sun, and K. D. Paulsen, "Application of the method of auxiliary sources to the wideband electromagnetic induction problem ", IEEE Transactions on Geoscience and Remote Sensing, Vol: 40 Issue: 4, Pages: 928 - 942, April 2002.

2. F. Shubitidze, K. O'Neill, S. A. Haider, K. Sun, and K.D. Paulsen, "Analysis of induction responses from metal objects using the method of auxiliary sources", Proceedings of 6th international conference on Mathematical Methods in Electromagnetic Theory, Pages: 468 - 470, 2000.

3. F. Shubitidze, K. O'Neill, and K. D. Paulsen "The method of auxiliary sources for analysis low frequency EM field scattering from composite objects". 2001 IEEE Antennas and Propagation Society International Symposium, Boston MA, Pages: 522 - 525, July 8-13, 2001.

4. F. Shubitidze, K. O'Neill, S. A. Haider, and K. D. Paulsen, "The method of auxiliary sources for analysis of low frequency electromagnetic induction sensor response" URSI National Radio Science Meeting, Boulder CO, Page 289, January 8-11, 2001.

5. F. Shubitidze, K. O'Neill, K. Sun, and K. D. Paulsen, "Investigation of broadband electromagnetic induction scattering by highly conducting, permeable, arbitrarily shaped 3-D objects" IEEE Transactions on Geoscience and Remote Sensing, in press.

6. F. Shubitidze, K. O'Neill, I. Shamatava, K. Sun, and K. D. Paulsen, "Implementation of hybrid MAS and SPA algorithm for broadband electromagnetic induction problems", VII-International Workshop on Direct and Inverse Problems of Electromagnetic and Acoustic Wave Theory (DIPED - 2002) , Tbilisi, Georgia, Pages: 33 - 37, October 10-13, 2002.

7. K. Sun, K. O'Neill, S. A. Haider, and K. D. Paulsen. "Numerical modeling of electromagnetic induction scattering from target with small but non-negligible skin depths". Proceedings of International Geoscience and Remote Sensing Symposium Honolulu, Vol. 4 1411 - 1414, July 24-28, 2000.

8. K. Sun, K. O'Neill, F. Shubitidze, S. A. Haider, and K. D. Paulsen, "Simulation of electromagnetic induction scattering from targets with negligible to moderate by primary fields," IEEE Transactions on Geoscience and Remote Sensing,, Vol: 40 Issue: 4, Pages: 910 - 927, April 2002.

9. K. Sun, K. O'Neill, F. Shubitidze, I. Shamatava, and K. D. Paulsen. " Theoretical analysis of TSA formulation and its domain of validity," submitted for publication in IEEE Transactions on Geoscience and Remote Sensing.

10. A. Krawczyk and J. A. Tegopoulos: "*Numerical Modeling of Eddy Currents*" Oxford science publications 1993.

11. D. Webster, *Aftermath; The Remnants of War*, Pantheon, NY, 1996.

12. B. Jonson, T. G. Moore, B. J. Blejer, C.F. Lee, T. P. Opar, S. Ayasli, and C. A. Prommerman, "A Research and development strategy for unexploded ordinance sensing", Lincoln Lab. Project. Rep. Lexington, MA EMP-1, 1996.

13. C. E Baum, "*Detection and Identification of Visually Obscured Targets*," Taylor and Francis 1998.

14. N. Geng, K. E. Baum, L. Carin. "On the low frequency natural responses of conducting and permeable Target." EEE Transactions on Geoscience and Remote Sensing, Vol. 37, Pages: 347 - 359, 1999.

15. L. Collins, P. Gao, J. Moulton, L. Makowsky, R. Weaver, D Keiswetter, I. J. Won. "Detection of low metal mines using frequency domain EMI." UXO forum 1999, Alexandria, Virginia May 24, 1999.

16. K. O'Neill, F. Shubitidze, I. J. Won, and D. Keiswetter, "Use of ultra-wideband spectroscopy to enhance electromagnetic induction discrimination". URSI National Radio Science Meeting, Boulder CO, Page 293 January 8 - 11, 2001.

17. J. T. Miller, T. H. Bell, J. Soukup, D. Keiswetter, "Simple phenomenological models for wideband frequency-domain electromagnetic induction" IEEE Transactions on Geoscience and Remote Sensing, Vol: 39 Issue: 6, Pages: 1294 – 1298, June 2001.

18. K. O'Neill, S. Haider, F. Shubitidze, K. Sun, C.O. Ao, H. Braunisch, and J. A. Kong, "Ultra-wideband electromagnetic induction spectroscopy", UXO Forum April 8-11, Florida, 2001.

19. A. R. Sebak, L. Shafai, and Y.Das, "Near zone fields scattered by three dimensional highly conducting permeable objects in the field of an arbitrary loop", IEEE Transactions on Geoscience Remote Sensing, Vol. 29. Issue 1, Pages: 9 – 15, January 1991.

20. I. J. Won, D. Keiswetter, T. H. Bell, "Electromagnetic induction spectroscopy for clearing landmines" IEEE Transactions on Geoscience Remote Sensing, Vol. 39. Issue 4, Pages: 703 -709, April 2001.

21. D. Keiswetter, I. J. Won, B. Barrow, T. H. Bell, " Object identification using multi-frequency EMI data". UXO forum 2000.

22. T. H. Bell, B. Barrow, and N. Khadr, "Shape-based classification and discrimination of subsurface objects using electromagnetic induction", IEEE Transactions on Geoscience and Remote Sensing, Vol: 39 Issue: 6, Pages: 509 - 513, June 2001.

23. P. Gao, L. Collins, P. Garber, N. Geng, L. Carin "Classification of landmine like metal targets using wideband electromagnetic induction ", IEEE Transactions on Geoscience Remote Sensing, Vol. 38. Issue 3. Pages: 1352 – 1361, May 2000.

24. L. Carin, Yu Haitao; Y. Dalichaouch, A. R. Perry, P. V. Czipott, C. E. Baum "On the wideband EMI response of a rotationally symmetric permeable and conducting target" IEEE Transactions on Geoscience and Remote Sensing,, Vol: 39 Issue 6, Pages: 1206 – 1213, June 2001

25. F. Shubitidze, K. O'Neill, K. Sun, and K. D. Paulsen, "Classification of scatterer's major axis aspect ratio using broadband EMI responses" International Union of Radio Science, National Radio Science Meeting, Page 271, Builder, Colorado, January, 9 - 12, 2002.

26. F. Shubitidze, K. O'Neill, K. Sun, and I. Shamatava "Application of broadband EMI responses to infer buried object's aspect ratio". 2002 IEEE Geoscience and remote sensing international symposium and 24-th Canadian symposium on remote sensing, Vol. 3, Pages: 1542 – 1545, Toronto, Canada, June 24 - 28, 2002.

27. K. Sun, K. O'Neill, F. Shubitidze, and K. D. Paulsen; "Treatment of broadband and multi-object electromagnetic induction scattering using high frequency approximations" 2002 IEEE Geoscience and remote sensing international symposium and 24-th Canadian symposium on remote sensing, Vol. 3, Pages: 1546 – 1549, Toronto, Canada, June 24 - 28., 2002.

28. I. Shamatava, K. O'Neill, F. Shubitidze, K. Sun, and C. Ao, "Evaluation of Approximate analytical solutions for EMI scattering from finite objects of different shapes and properties", 2002 IEEE Geoscience and remote sensing international symposium and 24-th Canadian symposium on remote sensing, Vol. 3, Pages: 1549 – 1552, Toronto, Canada, June 24-28., 2002.

29. L. M. Collins, Y. Zhang, and L. Carin "Model-Based statistical sensor fusion for unexploded ordnance detection". 2002 IEEE Geoscience and remote sensing international symposium and 24-th Canadian symposium on remote sensing, Vol. 3, Pages: 1556 –1559, Toronto, Canada, June 24-28., 2002.

30. F. Shubitidze, K. O'Neill, K. Sun and K.D Paulsen, " Analysis of UXO classification capability with the low frequency EMI sensor responses ". PIERS'2002 Progress In Electromagnetic Research Symposium, Page 44, Cambridge, MA, July 1 - 5, 2002.

31. J. R. Wait, "A conducting sphere in a time varying magnetic field'. Geophysics 16, Pages: 666-672, 1951a.

32. J. R. Wait and K. P Spies, "Quasi-static transient response of a conducting and permeable sphere'. Geophysics 34, Pages: 789 -792, 1969.

33. S. Ward and G. Hohmann, "Electromagnetic theory for Geophysical applications" In electromagnetic theory in Applied Geophysics. Tulsa OK: Soc. Exploration Geophysics, 1987.

34. H. Braunisch, C.O. Ao, K. O'Neill, and J. A. Kong, "Magnetoquasistatic response of conducting and permeable prolate spheroid under axial excitation". IEEE transactions on Geoscience and Remote Sensing, Vol: 39 Issue: 12 , Pages: 2689 – 2701, December 2001.

35. C.O. Ao H. Braunisch, K. O'Neill, J. A. Kong, "Quasi-magnetostatic solution for a conducting and permeable spheroid object to arbitrary excitation," Geoscience and Remote Sensing, IEEE Transactions on, Vol: 40 Issue: 4, Pages: 887 - 897, April 2002.

36. B. E. Barrowes, T. M. Grzegorczyk, J. A. Kong, K. O'Neill. "Broadband Analytical Solution of the Electromagnetic Induction (EMI) Response by Spheroidal Objects Under Arbitrary Excitation". PIERS-03, Page: 246, Honolulu, Hawaii, October 13 - 16, 2003.

37. C. D Moss, K. O'Neill, T. M. Grzegorczyk, and J. A. Kong, "A hybrid time domain method to calculate electromagnetic induction scattering from target with arbitrary skin depths", Proceedings of 19th Annual Review of Progress in Applied Computational Electromagnetics, Pages: 390 - 396, Monterey, CA, March 24 - 28, 2003.

38. F. Shubitidze, H. Anastassiu and D. Kaklamani, "An improved accuracy version of the method of auxiliary sources for computational electromagnetics" IEEE Transactions on Antennas and Propagations, in press.

39. F. Shubitidze, K O'Neill, K. Sun, and I. Shamatava, "Interaction between highly conducting and permeable metallic objects in the EMI frequency range," P Proceedings of 19th Annual Review of Progress in Applied Computational Electromagnetics, Pages: 625 - 631, Monterey, CA, March 24 - 28, 2003.

40. L. R. Passion and D. W. Oldenburg "Locating and Characterizing Unexploded Ordinance Using Time Domain Electromagnetic Induction ". ERDC/GSL TR-01-40 Technical report, August 2001.

41. I. J. Won, D. A Keiswetter, D.R. Hanson, E. Novikova and T. M. Hall, "GEM-3: a monostatic broadband electromagnetic induction sensor," Journal Environmental and Engineering Geophysics, Vol. 2, Issue 1, Pages: 53 - 64, 1997.

42. W. C. Chew, J. M. Jin, E. Michielssen, J. Song, 'Fast and Efficient Algorithms in Computational Electromagnetic ' Artech House, 2001.

43. F. Shubitidze, K. O'Neill, K. Sun, I. Shamatava and K. D. Paulsen. "Semi-analytical calculation of Jacobian in the electromagnetic inverse scattering problem," IEEE Antennas and Propagation Society International Symposium, Pages: 543 - 546 Columbus, OH, June 22-27, 2003.

Fridon Shubitidze received the degree of Diploma radio physicist (M.S) from the Sukhumi branch of Tbilisi State University, Republic of Georgia, in 1994 and Candidate of Sciences Ph.D degree in radio physics (applied electromagnetics) from its physics department, Tbilisi State University, Republic of Georgia, in 1997. Beginning in 1994 he was on the Research Staff of the Laboratory of Applied Electrodynamics, Tbilisi State University, Department of Physics, Republic of Georgia. At the same time he joined department of physics and mathematics, Sukhumi branch of Tbilisi State University as a senior teacher and became Associate Professor there in 1998. From 1998 to 1999 he held a postdoctoral fellowship in National Technical University of Athens, Greece, performing research in connection with computer simulation of electrostatic discharge, electrodynamics aspects of EMC, numerical modeling of conformal antennas, electromagnetic wave scattering, field visualization and identification of objects by scattered field analysis, investigation of wave propagation through anisotropy, plasma and chiral media; and innovative numerical methods. He is currently, working as Senior Research Associate at the Thayer School of Engineering, Dartmouth College, Hanover NH. His current work interests focus on numerical modeling of electromagnetic scattering by subsurface metallic objects.

Kevin O'Neill received the B.A. magna cum laude from Cornell University, followed by M.A., M.S.E., and Ph.D. degrees from Princeton University, Department of Civil Engineering. After an NSF postdoctoral fellowship at the Thayer School of Engineering at Dartmouth College and the U.S. Army Cold Regions Research and Engineering Laboratory (CRREL), he joined CRREL as a Research Civil Engineer. His research has focused on numerical modeling of porous media transport phenomena and of geotechnically relevant electromagnetic problems. He has been a Visiting Fellow in the Department of Agronomy at Cornell University, continues since 1989 as a Visiting Scientist at the Center for Electromagnetic Theory and Applications at MIT, and since 1984 has been on the adjunct faculty of the Thayer School. Current work centers on electromagnetic remote sensing of surfaces, layers, and especially buried objects such as unexploded ordnance.

Keli Sun received his B.S., M.S. and Ph.D. degrees in Computational and Biofluid Mechanics from the Department of Mechanics and Engineering Sciences, Peking University, Beijing, P. R. China, in 1991, 1994 and 1997 respectively. As an exchange student, he also worked in the school of Pure and Applied sciences, Tokyo University, Tokyo, Japan, from December 1995 to December 1996, studying the mobility and mechanical properties of membrane proteins in living cells. After getting his Ph.D. degree in 1997, he worked on the faculty of Tsinghua University, Beijing, P.R. China performing research and teaching biomechanics. He obtained a second Master of Science degree in Computational Electromagnetics in May 2001 from the Thayer School of Engineering at Dartmouth College in Hanover, NH. Dr. Sun is currently employed as a Research Associate in the Numerical Methods Laboratory in the Thayer School furthering his research in Computational Electromagnetics and its applications in remote sensing.

Irma Shamatava received the degree of Diploma radio physicist (M.S) from Sukhumi branch of Tbilisi State University, Republic of Georgia, in 1994. Since 1997, she has been on the Staff of the Computer center, Sukhumi branch of Tbilisi State University, Republic of Georgia. During the same period she joined Department of Physics and Mathematics, as an assistant teacher. She is currently, working as researcher at the Thayer School of Engineering, Dartmouth College, Hanover NH. Her research interests focus on analytical and numerical modeling of electromagnetic scattering by subsurface metallic objects.

Keith D. Paulsen received a B.S. from Duke University and M.S. and Ph.D. degrees from the Thayer School of Engineering, Dartmouth College, all in biomedical engineering. He was an assistant professor in electrical and computer engineering at the University of Arizona and jointly, an assistant professor in radiation oncology at the University of Arizona Health Sciences Center, and is now a professor of engineering at the Thayer School. A recipient of numerous academic and research awards and fellowships, he has carried out sponsored research for the National Science Foundation, the National Cancer Institute, the Whitaker Foundation, and the National Institute of Health. He has served on more than 10 advisory committees for the National Cancer Institute, and has chaired or organized five symposia on hyperthermic cancer treatment. He has published over 60 journal articles, over three dozen conference presentations, abstracts, and papers, and contributed chapters on electromagnetic power deposition patterns to five books. At Thayer School he is co-founder and co-manager of the Numerical Methods Laboratory. He performs research and teaches courses in computational methods for engineering and scientific problems, with particular applications in electromagnetics, subsurface object sensing, and biomedical engineering.